

Hard X-ray Properties of the Merging Cluster Abell 3667 as Observed with *Suzaku*

Kazuhiro NAKAZAWA,

Department of Physics, The University of Tokyo, 7-3-1 Hongo, Bunkyo-ku, Tokyo 113-0033

E-mail(KN) : nakazawa@amaltha.phys.s.u-tokyo.jp

Craig L. SARAZIN,

Department of Astronomy, University of Virginia, P.O. Box 400325, Charlottesville, VA 22904-4325

Madoka KAWAHARADA,

Cosmic Radiation Laboratory, RIKEN, 2-1 Hirosawa, Wako, Saitama 350-0198

Takao KITAGUCHI, Sho OKUYAMA, Kazuo MAKISHIMA,

Department of Physics, The University of Tokyo, 7-3-1 Hongo, Bunkyo-ku, Tokyo 113-0033

Naomi KAWANO, Yasushi FUKAZAWA,

Department of Physical Science, Hiroshima University, 1-3-1 Kagamiyama, Higashi-hiroshima 739-8526

Susumu INOUE,

Department of Physics, Kyoto University, Kyoto, Oiwake-cho, Kitashirakawa, Sakyo-ku, Kyoto 606-8502

Motokazu TAKIZAWA,

Department of Physics, Yamagata University, 1-4-12 Kojirakawa-machi, Yamagata 990-8560

Daniel R. WIK,

Department of Astronomy, University of Virginia, P.O. Box 400325, Charlottesville, VA 22904-4325

Alexis FINOGENOV,

Max-Planck-Institut für Extraterrestrische Physik, Giessenbachstraße, 85748 Garching, Germany

also University of Maryland, Baltimore County, 1000 Hilltop Circle, Baltimore, MD 21250, USA

and

Tracy E. CLARKE

Naval Research Laboratory, 4555 Overlook Ave. SW, Code 7213, Washington D.C. 20375

also Interferometrics Inc., 13454 Sunrise Valley Drive, Suite 240, Herndon, VA 20171

(Received ; accepted)

Abstract

Wide-band *Suzaku* data on the merging cluster Abell 3667 were examined for excess hard X-ray emission. *Suzaku* detected X-ray signals in the wide energy band from 0.5 to 40 keV. The hard X-ray (> 10 keV) flux observed by the HXD around the cluster center cannot be explained by a simple extension of the thermal emission with average temperature of ~ 7 keV. The emission is most likely an emission from a very hot ($kT > 12.9$ keV) thermal component around the cluster center, produced

via a strong heating process in the merger. In the north-west radio relic, no signature of non-thermal emission was observed. Using the HXD, the overall upper-limit flux within a $34' \times 34'$ field-of-view around the relic is derived to be 5.5×10^{-12} erg $\text{s}^{-1} \text{cm}^{-2}$ in the 10–40 keV band, after subtracting the ICM contribution estimated using the XIS or the *XMM-Newton* spectra. Directly on the relic region, the upper limit is further tightened by the XIS data to be less than 6.8×10^{-13} erg $\text{s}^{-1} \text{cm}^{-2}$, when converted into the 10–40 keV band. The latter value suggest that the average magnetic field within the relic is higher than $1.6 \mu\text{G}$. The non-thermal pressure due to magnetic fields and relativistic electrons may be as large as $\sim 20\%$ of the thermal pressure in the region.

Key words: X-rays: galaxies: clusters: individual (Abell 3667) — radiation mechanisms: non-thermal

1. Introduction

Enigmatic extended radio sources in rich galaxy clusters have been known for over 30 years (Willson 1970; for recent review, see Feretti 2005). Sources located at the cluster center are referred to as “radio halos”, while those on the cluster periphery are called “relics”. Steep spectra and spectral cutoffs at a few GHz detected in several halos/relics indicate that relativistic electrons with typically GeV energy are undergoing cooling due to synchrotron and inverse Compton (IC) emission. In every case, the radio halos/relics are found in irregular clusters which are apparently undergoing mergers. This suggests that the radio emitting electrons are accelerated by shocks or turbulence generated by energetic cluster merging.

The same relativistic electrons scatter Cosmic Microwave Background (CMB) photons up to the hard X-ray band (IC emission). By comparing the radio and the hard X-ray emissions, not only the electron energy density but also the intra-cluster magnetic field intensity can be estimated (e.g. Sarazin 1988). Detecting the IC emission is difficult because of the strong ICM component dominant below ~ 20 keV and the low expected flux of the emission in hard X-rays above this energy. Currently, there are only a few reports claiming its detection, mostly from the *Beppo-SAX* PDS in the energy band around 40 keV or higher (e.g. Fusco-Femiano et al. 1999; Nevalainen et al. 2004), though a few of the detections are still controversial (Rossetti & Molendi 2004; Fusco-Femiano et al. 2007). Another case includes the *ASCA* GIS results around 4 keV on galaxy groups (Fukazawa et al. 2001; Nakazawa et al. 2006). These results would require a magnetic field as low as $0.1 \mu\text{G}$ (e.g. Fusco-Femiano et al. 1999), which at the first glance is inconsistent with the radio rotation measure estimation of $2 \sim 10 \mu\text{G}$ (e.g. Clarke et al. 2001; Carilli & Taylor 2002). Further observations by independent instruments of IC and other hard X-ray emission processes (e.g. Inoue et al. 2005), is thus desirable.

Significant heating of the ICM itself must also be taking place in merging clusters (e.g.

Takizawa 2000). X-ray hardness ratio images sometimes show temperatures exceeding 10 keV (e.g. Watanabe et al. 1999, Briel et al. 2004). Since the emission can be multi-phase within the line of sight, the actual highest temperature can be much higher, though it is not easy to identify using the contemporary imaging X-ray detectors working below < 12 keV.

In many ways, Abell 3667 is the ideal cluster to study mergers, radio relics and hard X-ray emission. It is a very bright X-ray cluster at a low redshift of $z = 0.0556$ (Struble & Rood 1999). The *ROSAT* and *ASCA* observations showed that it is a spectacular merger with shock heated gas (Markevitch et al. 1999). *Chandra* and *XMM-Newton* observations have shown much evidence for an ongoing merger, such as a cold front (Vikhlinin et al. 2001a,b) and highly inhomogeneous temperature structure with temperature ranging from 4 to > 10 keV (Mazzotta et al. 2002; Briel et al. 2004). The optical galaxy distribution shows elongation towards the north-west south-east axis (Sodre et al. 1992; Johnston-Hollitt et al. 2008), supporting the binary merger scenario as well.

The cluster is famous for its pair of radio relics (e.g. Roettgering et al. 1997). The relic to the north-west is the brightest and largest among the diffuse radio sources associated with cluster of galaxies, having a flux of 3.7 Jy (Johnston-Hollitt 2004) and a width of $\sim 20'$ at 1.4 GHz. It is located about $30'$ or 2 Mpc from the cluster center. The radio signal is detected from 85 MHz to 2.3 GHz, and its average photon index is $\Gamma = 2.1$ (Roettgering et al. 1997). Here the photon index Γ is defined as $N_{\text{photon}}(E) = N_0 \times E^{-\Gamma}$. The radio relics have very sharp outer edges and the radio spectra steepen with distance from the edge. Thus, the radio relics are considered to reflect the position of the particle acceleration in a merger shock. The cluster is also a good candidate for detection of IC emission. The *Beppo-SAX* PDS provided a rather marginal evidence of hard excess emission from the cluster (Fusco-Femiano et al. 2001; Nevalainen et al. 2004). However, the large field of view (FOV) of the PDS makes the data strongly affected by contamination from thermal emission from the entire cluster, mainly from its central region, and possible AGNs.

The hard X-ray detector (HXD; Takahashi et al. 2006; Kokubun et al. 2006) onboard *Suzaku* (Mitsuda et al. 2006) is characterized by its low detector background in the 10–40 keV band and its narrow FOV of $34'$ full width at half maximum (FWHM). Using the HXD, we can spatially distinguish hard X-ray components from the cluster center and the north-west relic, with the highest sensitivity in the 10–40 keV band. In addition, the X-ray CCD cameras (XISs; Koyama et al. 2006) onboard *Suzaku* are characterized by their large effective areas and low and stable detector backgrounds, which make them very powerful devices to observe extended hard emission.

In May 2006, we observed Abell 3667 cluster using *Suzaku* with three pointings running from the north-west relic to the center, each separated by $\sim 17'$. Here we report the results obtained by these observations. Observation logs and data reduction are described in the next section. Section 3 is devoted to the spectral and imaging analysis, followed by the discussion

in section 4 and conclusions in section 5. In this paper, we utilized canonical cosmology value of $H_0 = 70 \text{ Mpc km}^{-1}\text{s}^{-1}$. At the redshift of $z = 0.0556$, $1'$ corresponds to 62 kpc. For a mean cluster temperature of 7.2 keV, the virial radius should be $r_{200} \sim 2.6 \text{ Mpc} = 42'$ (e.g. Neumann & Arnaud 1999). Unless otherwise noted, all errors are at the 90% confidence limit.

2. Observation and Data Reduction

2.1. Observation logs

Table 1. Log of the three Abell 3667 observations.

Obs.	Start (UT)	End (UT)	Exp. (ks) *
NW_Relic	05/03 17:47	05/06 07:02	81.2/45.6
NW_17off	05/06 07:03	05/06 17:39	16.7/11.4
Center	05/06 17:40	05/07 09:13	20.5/7.2

* The XIS/HXD exposure time after the screening as presented in the text.

The three Abell 3667 pointing observations of *Suzaku* were carried out successively in the beginning of May 2006. As already noted, individual pointing positions are offset by $\sim 17'$, so that the first observation covers the north-west relic, and the last one on the cluster center, with continuous XIS coverage. Hereafter, we call these observations, the NWR, the 17' offset and the center pointing, respectively. Details of the observation time are summarized in table 1.

The XIS was operated in the normal timing and full window mode. All the 64 PINs of the HXD were operated in the nominal bias voltage of 500 V. All the data was processed with the *Suzaku* pipeline processing of version 2.0.6.13.

2.2. Data reduction of the XIS

2.2.1. Screening and background estimation

The XIS data were processed via default screening criteria. Events with a GRADE of 0, 2, 3, 4, 6 and STATUS < 65536 were extracted. Data screening criteria with HK files are as follows: time after SAA (T_SAA_HXD) > 436 s, the new cut-off rigidity (COR2) > 6.0 GV, elevation from the earth rim > 5° and that from the sun-lit earth rim > 20° . Non X-ray background (NXB) spectra of the XIS were created by sorting night earth data by COR2, and weighted-averaging them using the ftool “xisnxbgen” (Tawa et al. 2008). The estimation uncertainty in the NXB level is handled as a systematic error in the following analysis. Tawa et al. (2008) studied the error on a typical observation lasting for a few days. At the 90% confidence level, it is 6.0% and 12.5% for the sum of three XIS-FI (XIS-0,2,3) data and the BI (XIS-1) data, respectively.

Another major background is the Cosmic X-ray background (CXB). Details of the CXB

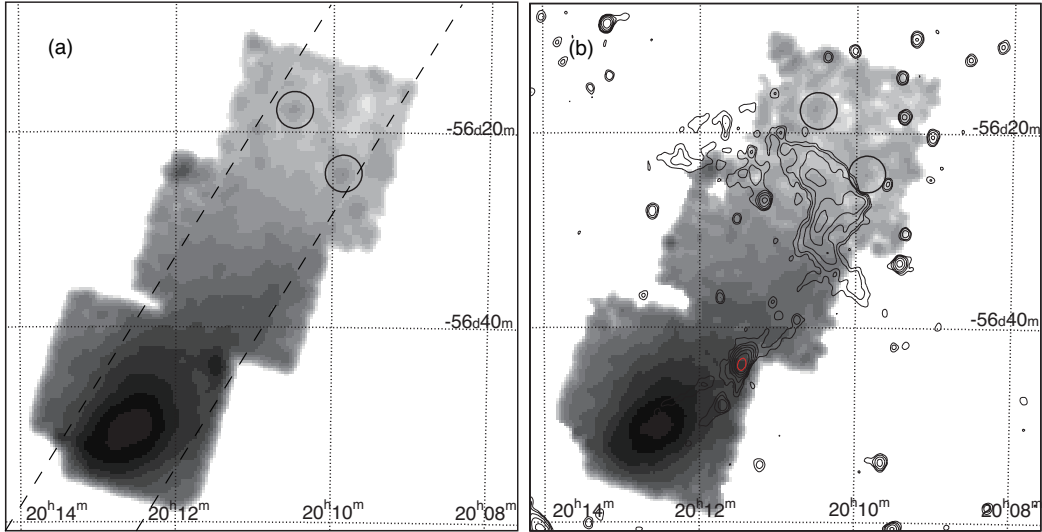


Fig. 1. Mosaic XIS image of the three pointing observations, in (a) the soft 1-4 keV band and (b) the hard 4-8 keV band. See text for details. The images are smoothed by a Gaussian kernel with $\sigma = 0.5$ arcmin. Gray-scale contours are logarithmically scaled by a factor of 1.5. In the hard band image, the 843 MHz radio image (by SUMSS) is overlaid as a thin contour. Two point source candidates are shown as open circles in the NWR region, and the projection analysis band is shown as a dashed lines in panel (b); both are discussed later in section 3.4.3.

estimation is shown in appendix 1. Because the whole XIS region in all the three observations could be filled with non-thermal or thermal diffuse emission, we used the Lockman Hole observation (*Suzaku* observation ID, 101002010) as the CXB template. In addition, the northern 1/3 of the NWR pointing data was utilized for foreground Galactic soft thermal component modeling. The CXB fluctuation is estimated to be 11% over the XIS full FOV. Hereafter, we treat the background-subtracted (both the NXB and CXB) spectra as signals from Abell 3667.

2.2.2. The XIS image

In figure 1, we show 1–4 keV and 4–8 keV XIS-FI mosaic images of the three pointings. After co-adding the images from XIS-0, 2 and 3, they were corrected for the overlapping exposure, and for vignetting effect of the mirror optics, after subtracting the NXB. Thanks to the wide energy range and low background of the XIS, we can see signals even in the NWR region which is 30' (2 Mpc) away from the X-ray centroid. On the other hand, no apparent emission associated with the radio relic is seen in neither band image. Detailed analysis using these images is performed in section 3.4.3.

2.3. Data reduction of the HXD

2.3.1. Screening and background estimation

We processed the uncleaned event files of the HXD with “hxdgtigen”, and remaining events were further screened with HK files as follows; time after SAA (T_SAA_HXD) > 500 s,

the COR2 > 8.0 GV and elevation from the earth rim > 5°. As the NXB of the PIN, we utilized public NXB model which is provided by the HXD team in the *Suzaku* website¹. The version of the model is “METHOD=LCFITDT”, or “tuned”. Observations of Abell 3667 was carried out in a period in which the lower threshold of the scintillator was set low, and the dead time caused by the data transfer overflow between the HXD’s analog and digital electronics is large. This phenomena in principle is considered not to affect the dead time correction significantly. Since the HXD data in this paper, however, is dominated by the systematic error and not statistics, and most of the systematic error analysis is performed in periods excluding these phenomena, we stick to the original cleaned criteria. Note that almost no difference happens if we utilize those periods with the data transfer overflow.

In the HXD-PIN NXB documents (Fukazawa et al. 2008; Mizuno et al. 2008²), the reproducibility of blank-sky observations separated into 10 ks exposures gave a distribution of 3.5% in 1σ , including the statistical error of typically 1.9% or larger and the CXB fluctuation of 1.3%, as described later. This gives a systematic uncertainty of 2.6% in 1σ , or 4.3% at the 90% confidence. In the following analysis, we utilized this value as the systematic error of the NXB. Because 10 ks is a bit shorter than the exposure of our observations, actual systematic error is supposed to be slightly smaller than this value.

Detail of the CXB model used for the PIN is described in appendix 2. We defined the photon flux model as $N(E) = 8.69 \times 10^{-4} \times (E)^{-1.29} \times \exp(-E/40.0)$ in photons $\text{cm}^{-2} \text{s}^{-1} \text{keV}^{-1} \text{FOV}^{-1}$. Here, E is the photon energy in keV, and the model is normalized to the HXD-PIN opening angle (or FOV) of $\Omega_e^{\text{HXD}} = 0.32 \text{ deg}^2$, to be combined with the HXD nominal response. The 13.2% systematic difference of the XIS and PIN (Ishida et al. 2007)³ is also accounted in the following fitting process. The level of the CXB fluctuation is calculated to be 18%, which corresponds to 1.3% of the CXB+NXB in the 10-40 keV band.

We also checked whether the PIN data suffered from thermal noise in the lower energy band by comparing the actual earth occultation data with the corresponding model NXB spectra. Since the detector temperature was relatively high at -12 C° in these observations, the thermal noise is seen as a steep rise below 13 keV. In the higher energy band, the two spectra are consistent within statistics.

2.3.2. Signals of the three pointings

In figure 2, the 13–40 keV band light curves of PIN for a total of 4 days of observations are presented. The PIN background varies by $\sim 25\%$, mainly correlated with COR, and time elapsed after a passage of SAA (T_SAA_HXD). The PIN residual signal clearly exceeds the CXB level for all three observations. Note that the flux increases towards the cluster center.

¹ <http://www.astro.isas.jaxa.jp/suzaku/analysis/hxd/pinnxb/>

² *Suzaku*-memo, JX-ISAS-SUZAKU-MEMO-2008-03.

³ *Suzaku*-memo, JX-ISAS-SUZAKU-MEMO-2007-11.

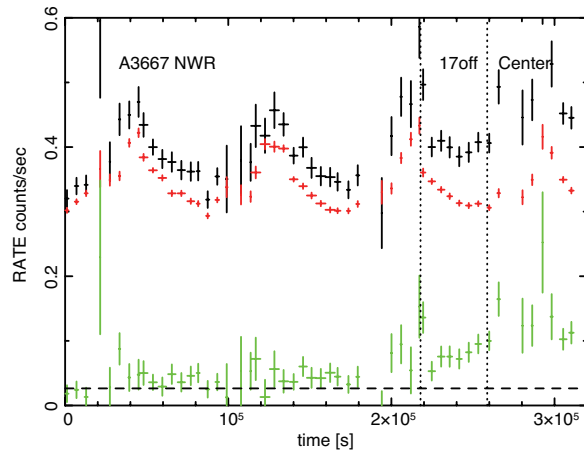


Fig. 2. The HXD light curves in the 13-40 keV range. Black crosses stands for the data, red for the background model and green for the residual signals. Time regions of the three observations are separated by vertical dotted lines. The horizontal dashed line indicates the expected CXB rate.

Small variations seen in the residual signal are due to uncertainties in the NXB modeling in this rather short time bin (90 minutes), and the NXB-subtracted count rate is consistent with being constant within each pointing.

In Figure 3, we show raw PIN spectra from the 3 observations, together with the NXB model spectra. Difference between the two spectra are also presented, and compared to the CXB model. In all cases, the NXB-subtracted data significantly exceeds the CXB. The signal is strongest in the center pointing, and weakest in the NWR pointing. The 13–40 keV PIN signal rates are $(8.2 \pm 1.3, 5.2 \pm 0.9 \text{ and } 1.2 \pm 0.5) \times 10^{-2} \text{ cts s}^{-1}$ in the center, the 17' offset, and the NWR data, respectively. The systematic error is $1.4 \times 10^{-2} \text{ cts s}^{-1}$, when evaluated as a quadrature sum of those of the CXB and the NXB. Thus, we can claim the signal detection from Abell 3667 up to 30 keV both in the center and 17' offset observations.

We also estimated the point-source contribution to the HXD-PIN using the *ROSAT*-PSPC and the *ASCA*-GIS data. In short, we confirmed that the contribution from these sources is less than 10% and hence almost negligible. Details are shown in appendix 3.

2.4. Preparation of arf files of the *XIS* and the *PIN*

When trying to quantify the brightness and spectral shape of the PIN signals, we need to know the angular transmission (or effective area) of PIN to the corresponding hard X-ray emission. This in turn requires knowledge of the location and shape of the source, which is unavailable in the PIN energy range. In evaluating the ICM contribution to the PIN band, we therefore assumed it to have the same spatial distribution as the ICM signals detected with the PSPC, as a plausible approximation. Then, we calculated the PIN arf file by convolving the point source arf corresponding to the specified sky region multiplied by the relative PSPC image intensity map. See Kitaguchi et al. (2008) for detailed description of the arf generation.

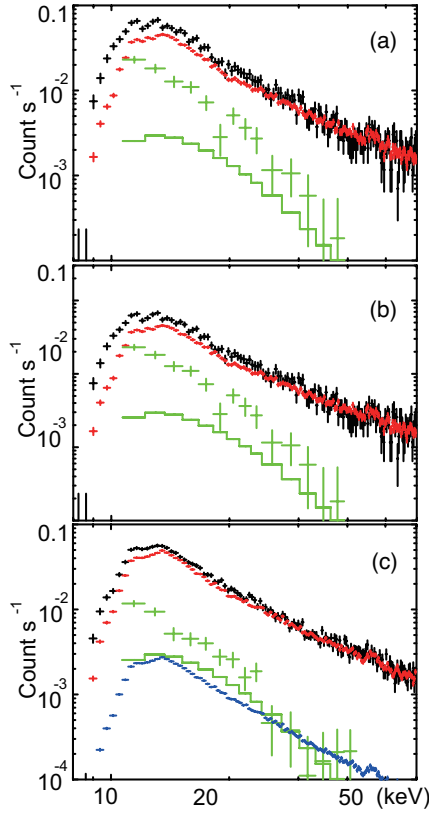


Fig. 3. PIN spectra of the three pointings, from (a) center, (b) 17' off and (c) NWR. Black crosses stand for the data, red for the NXB model and green for the residual signals (data – NXB). The expected CXB spectra are also plotted as green histograms. Typical systematic errors due to the CXB fluctuations and the NXB reproducibility are shown in the NWR data in blue.

Note that the energy response has in principle negligible dependence on the position within the FOV. The cross-normalization factor of 1.132 between the PIN and the XIS is incorporated, as well.

Interestingly, the count-rate ratios to the center pointing predicted from the synthesized arf files are 0.61 and 0.14 for the 17' offset and the NWR pointings, respectively. This value matches the actually observed ratios, 0.60 and 0.11, respectively, within the statistical error. In other words, we confirmed that contribution from the cluster central region to the PIN data of the NWR pointing is not negligible. As a reference, those of a point source located at the cluster X-ray centroid are 0.42 and 0.05, respectively.

In a similar way, we synthesized the XIS arf files with the ftool “xissimarfgen”, using the PSPC image as an input. Since the NWR region is around the detection limit of both the PSPC and the XIS, the arf files for this region could be inaccurate, and they require special care in the following analysis. This effect is negligible in the center and 17' offset pointings because of the high X-ray surface brightness.

To confirm the accuracy of the generated arf files, we first compared the XIS results

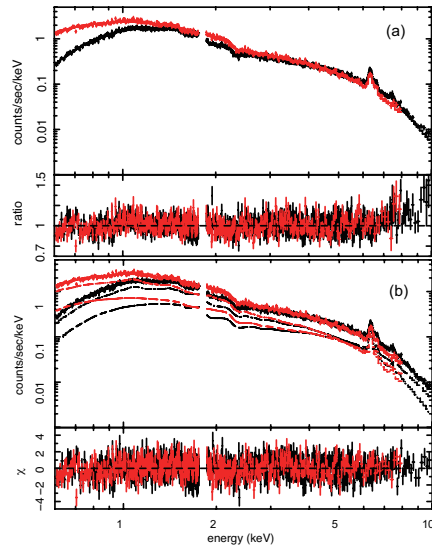


Fig. 4. The XIS-FI (black) and XIS-BI (red) center spectra, fitted with (a) $1kT$ and (b) $2kT$ thermal emission model.

to those of the PSPC. The 0.5–2.0 keV ICM flux derived from the PSPC (Mohr et al. 1999) accumulated within 30' from the X-ray centroid is about 8% smaller compared to the results obtained from the XIS data. Thus, the XIS arf is assumed to be accurate within $\sim 10\%$ in its absolute flux. On the other hand, the XIS and PIN calibration is verified within $\sim 3\%$ accuracy using the Crab observations, including the mapping within the PIN-FOV. Because the PIN-FOV is relatively simple in its shape, no strong systematic error is expected. Using the similar approach, the PIN spectra of the Abell 1060, Centaurus (Kitaguchi et al. 2008) and Coma clusters (Wik et al. 2008) were reproduced successfully by extrapolating the XIS or *XMM* spectra. From these results, we conservatively assume a 10% uncertainty in the *relative* normalization of the XIS and the PIN arf files.

3. Wide-band spectral analysis

3.1. Spectral properties of the central pointing

With the preparation made in section 2, we proceed to the spectral analysis of the XIS and the PIN. The central pointing afforded the signal detection with the highest significance using both instruments. Their arf files are also the most reliable since the brightest central emission is well detected by the PSPC. Thus, we started the spectral fitting from the central pointing. We first start with evaluating the XIS and the PIN spectra individually, and then performed the combined fitting. Here, the XIS-FI, the XIS-BI and the PIN spectra are utilized in 0.6–10.0 keV, 0.6–8.0 keV, and 13–40 keV, respectively.

Table 2. Best fit parameters of the $1kT$ and $2kT$ models fitted to the center XIS spectra.

	$1kT$	$2kT$
kT_{low}^*	6.8	$4.70^{+0.28}_{-0.34} \quad ^{+0.06}_{-0.04}$
kT_{hi}^\dagger	–	$21.4^{+8.0}_{-5.4} \quad ^{+1.3}_{-2.2}$
Z_{O}^\ddagger	0.55	$0.47^{+0.17}_{-0.17} \quad ^{+0.01}_{-0.03}$
Z_{Si}^\S	0.21	$0.33^{+0.11}_{-0.12} \quad ^{+0.01}_{-0.01}$
Z_{Fe}^\parallel	0.33	$0.39^{+0.03}_{-0.03} \quad ^{+0.00}_{-0.00}$
$N_{\text{low}}^\#$	9.2×10^{-2}	$6.2^{+0.6}_{-0.8} \quad ^{+0.1}_{-0.0} \times 10^{-2}$
$N_{\text{hi}}^\#$	–	$3.5^{+0.6}_{-0.5} \quad ^{+0.1}_{-0.1} \times 10^{-2}$
$\chi^2/\text{d.o.f.}$	1133.0/1002	1033.9/1000

* Temperature of the (cooler) thermal component in the $1kT$ ($2kT$) fit, in keV. Errors are 90% statistical and systematic, respectively, latter evaluated by shifting the NXB and CXB within their systematic errors.

† Temperature of the hotter thermal component in the $2kT$ fit.

‡ Metal abundance of O, Ne, Mg and Al.

§ Metal abundance of Si, S, Ar and Ca.

∥ Metal abundance of Fe and Ni.

Normalization in the *apecc* code, for the low and high temperature components.

3.1.1. The XIS

Spectra from the three XIS-FI chips are summed up to form a single XIS-FI spectrum. Since the XIS-BI chip has a significantly different detector response, its spectra is separately handled. The arf files prepared in section 2.4 are used for the XIS-FI, XIS-BI and the PIN data. In the following fitting procedures, the relative normalization between the two (FI and BI) XIS data sets is set free, to adjust for residual calibration uncertainties between them which are about 3% or less. Since the data have very high statistics, the energy range of 1.76–1.86 keV in the XIS spectra were ignored to avoid uncalibrated structures caused by the Si edge. The XIS-FI and BI spectra are grouped so that each energy bin has at least 200 counts.

We first applied a single temperature thermal emission model (hereafter $1kT$ model) to the XIS spectra, utilizing the *vapecc* code in the XSPEC (v11.3.2) software package. Galactic absorption was modeled by the *wabs* code with a fixed column density of $4.7 \times 10^{20} \text{ cm}^{-2}$, as derived by the radio observations (Dickey & Lockman 1990). The redshift was also fixed at $z = 0.0556$. Metal abundances are grouped into three; O, Ne, Mg and Al as the first group, Si, S, Ar and Ca as the second one, and Fe and Ni as the third one. Their relative ratios refer to Anders & Grevesse (1989). The temperature and the normalization were also set free.

Fit with the $1kT$ model was unsuccessful with $\chi^2/\text{d.o.f.} = 1133.0/1002$, leading to null hypothesis probability of 2.4×10^{-3} . The fitted temperature was about 6.8 keV, which is generally consistent with temperatures given in the literature (e.g. Fukazawa et al. 2004).

Figure 4 presents the data compared to the best fit model. In the $1kT$ fitting, residuals around 1 keV and above 8 keV are significant. Even if we set the N_{H} free, the fit did not improved significantly, suggesting the thermal component modeling itself needs improvement.

Considering the multi-temperature nature of the cluster (e.g. Briel et al. 2004), we added another thermal component. Metal abundances of the two *vapex* components were tied to be the same, and only the temperature and normalization set free (hereafter $2kT$ model). The fit improved significantly and became acceptable with $\chi^2/\text{d.o.f.} = 1033.9/1000$ or null hypothesis probability of 22%. Here, we also estimated the systematic error by shifting both the NXB and CXB to their highest and lowest possible value at 90% confidence. The shifts observed in the fitted central value are quoted as systematic uncertainty. In this fitting, the hotter component temperature is suggested to be higher than 15.6 keV. Here (and in all of the following analysis), the errors are derived as a quadrature sum of the statistical and the systematic ones when obtaining the final result, while the two components are separately presented in the tables for clarity. When fitted using a model with a thermal and a power-law component (hereafter $1kT + PL$ model), the fit also improves providing $\chi^2/\text{d.o.f.} = 1056.8/1000$ or null hypothesis probability of 9.6%. The photon index derived is hard with $\Gamma = 1.0_{-0.8}^{+0.2}$. The shape of the power-law or hotter component is very hard, so that it is not easy to restrict only with the XIS energy band, below ~ 10 keV.

3.1.2. The HXD-PIN

The signal detected by the PIN is significant compared to any possible systematic errors. We then studied the shape of the PIN spectrum in the 13–40 keV range. The spectra are grouped into fixed 12 bins, each with sufficient counts. When we simply fit a power-law model to the PIN spectrum, the resultant photon index Γ is as soft as 3.5. If we try the $1kT$ model with metal abundances fixed at 0.3, the resultant temperature is derived as ~ 8.5 keV. Detailed results are presented in table 3. At the first glance, no strong signature of spectrally hard component is suggested in the PIN spectra. We also note that, although the error bar is large because of both the statistical and systematic errors, the photon index Γ is softer than those suggested from the radio observation, i.e. $\Gamma \approx 2.1$ and the XIS spectral fitting with $1kT + PL$ model. On the other hand, the PIN flux level provides important results, as shown in the next section.

3.1.3. Combined XIS-HXD analysis

Following the spectral analysis individually performed to the XIS and the PIN, in this section we give the results of a wide-band spectroscopic analysis, using the two spectra combined (the XIS+PIN combined spectra). We utilized the arf files generated in section 2.4, and fixed the normalization of the XIS-FI and the PIN spectra.

We first applied the $1kT$ model. Procedures and fitting parameters are the same to those of the XIS-only analysis. The fit again gave a temperature of ~ 6.9 keV. However, as

Table 3. Spectral parameters fitted to the HXD spectra of the center pointing in the 13–40 keV range.

	Γ or kT^*	flux or norm [†]	$\chi^2/\text{d.o.f.}$
PL model	$3.6^{+1.0}_{-0.8}$ $^{+0.5}_{-0.3}$	32^{+5}_{-5} $^{+6}_{-5}$	6.3/10
$1kT$ model	$8.5^{+5.6}_{-2.9}$ $^{+1.7}_{-1.7}$	$7.9^{+12.0}_{-4.1}$ $^{+2.0}_{-1.1}$	6.2/10

* Photon index Γ or thermal component temperature (in keV) of the power-law or $1kT$ fitting, respectively.

† The 10-40 keV flux of the power-law component, in 10^{-12} erg s⁻¹ cm⁻², or the normalization in apec model, for the low and high temperature components.

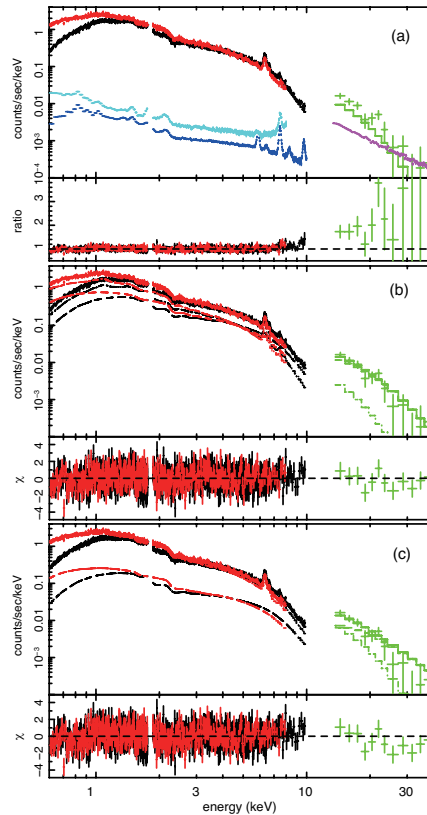


Fig. 5. Wide-band spectra of the center pointing, fitted with the (a) $1kT$, (b) $2kT$ and (c) $1kT + PL$ model. In the panel (a), typical 90% confidence systematic error in the NXB and CXB are also shown for reference, in cyan, blue and magenta corresponding to the XIS-FI, BI and PIN, respectively. Panel (a) is shown together with the residual ratio, while the other two are with the delta-chi distribution.

shown in figure 5 (a), the $1kT$ model failed to explain the PIN data, as well as the XIS data in the energy band above 7 keV. As a result, the fit is unacceptable with $\chi^2/\text{d.o.f.} = 1165.4/1014$. What is more, the observed PIN counts are about a factor of 2 larger than the best-fit $1kT$ model. This excess is larger than any possible calibration errors in the arf, which are at the $\sim 10\%$ level, and any systematic error associated with the NXB and CXB, as well.

To characterize the hard excess, we next applied the $2kT$ model. As shown in figure 5 (b) and table 4, a good fit with $\chi^2/\text{d.o.f.} = 1044.4/1012$ was obtained. Interestingly, both

Table 4. The best fit parameters of the $2kT$ and $1kT + PL$ models fitted to the XIS+PIN combined spectra of the center pointing. Columns are similar to those shown in table 2.

	$2kT$	$1kT + PL$
kT_{low}	$4.68^{+0.30}_{-0.38} \quad ^{+0.00}_{-0.06}$	$6.05^{+0.19}_{-0.19} \quad ^{+0.22}_{-0.28}$
kT_{hi}	$18.5^{+4.8}_{-3.8} \quad ^{+4.8}_{-4.1}$	–
Z_{O}	$0.47^{+0.17}_{-0.17} \quad ^{+0.01}_{-0.02}$	$0.47^{+0.19}_{-0.19} \quad ^{+0.00}_{-0.01}$
Z_{Si}	$0.32^{+0.12}_{-0.12} \quad ^{+0.00}_{-0.01}$	$0.29^{+0.14}_{-0.13} \quad ^{+0.01}_{-0.01}$
Z_{Fe}	$0.39^{+0.03}_{-0.03} \quad ^{+0.01}_{-0.00}$	$0.35^{+0.03}_{-0.02} \quad ^{+0.01}_{-0.01}$
N_{lo}	$6.0^{+0.6}_{-0.9} \quad ^{+0.1}_{-0.4} \times 10^{-2}$	$8.2^{+0.5}_{-0.5} \quad ^{+0.4}_{-0.4} \times 10^{-2}$
N_{hi}	$3.7^{+0.9}_{-0.6} \quad ^{+0.2}_{-0.1} \times 10^{-2}$	–
Γ_{PL}^*	–	$1.36^{+0.12}_{-0.18} \quad ^{+0.00}_{-0.02}$
F_{PL}^\dagger	–	$38^{+7}_{-7} \quad ^{+13}_{-14}$
$\chi^2/\text{d.o.f.}$	1044.4/1012	1088.0/1012

* Photon index of the power-law component.

† 10–40 keV flux of the power-law component, in $10^{-12} \text{ erg s}^{-1} \text{ cm}^{-2}$.

the XIS and the PIN excess *consistently* disappeared, although the mutual normalization is fixed using the arf file generated according to the PSPC image profile. Considering both the statistical and systematic errors (table 4), this hard component, if interpreted as thermal, is characterized by a temperature of kT_{hi} ranging from 12.9–25.3 keV.

As another candidate, we fitted the $1kT + PL$ model to the XIS+PIN combined spectra. The fit was improved compared to the $1kT$ model, and marginally acceptable giving 4.8% in null hypothesis probability. As shown in table 4, the photon index was hard with $\Gamma = 1.4$ and the inferred power-law flux in 10–40 keV was $\sim 4 \times 10^{-11} \text{ erg s}^{-1} \text{ cm}^{-2}$.

Through the analysis on the XIS+PIN combined spectra of the central pointing, we conclude that the excess hard component suggested in the XIS data is clearly required in the PIN spectra as well. The emission is likely to be of thermal origin, a very hot component with temperature exceeding 12.9 keV, or less likely a hard ($\Gamma \sim 1.5$) power-law component. We also checked the Fe-K line profile, and found that it was consistent with both the $1kT + PL$ and the $2kT$ interpretations. In any case, the analysis of the other observations, i.e. the 17' offset and the NWR pointings, will be helpful to identify the origin of the hard emission. The XIS and PIN data in these pointings contains spatial information of the excess component. What is more, the strong north-west radio relic is observed with the deep (81 ks in the XIS) NWR pointing.

3.2. Spectral properties of the offset pointings

When analyzing the offset pointings, we have to take into account that, although the XIS spectra are of local origin (from within the FOV), the PIN spectra is largely contaminated from

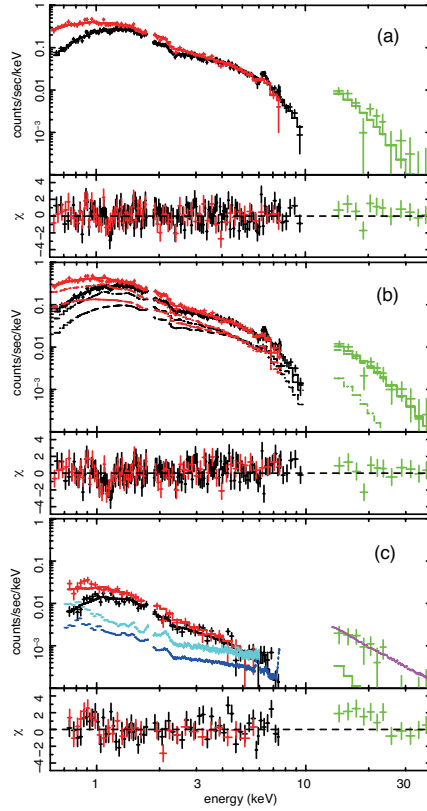


Fig. 6. Wide-band spectra of (a) the 17' offset pointing fitted with $1kT$ model, (b) plotted with $2kT$ best-fit model of the central pointing. (c) The NWR spectra with the $1kT$ best-fit model to the XIS. Cyan, blue and magenta plots show the typical systematic error of the XIS-FIs, BI and the PIN spectra. See text for details.

Table 5. Similar to table 4, but for the 17' off and the NWR offset spectra fitted with the $1kT$ model.

	17' off*	NWR†
kT [keV]	$7.75^{+0.32}_{-0.33} \quad +0.36_{-0.51}$	$3.6^{+0.4}_{-0.4} \quad +0.5_{-0.6}$
Z_{O}	$0.69^{+0.79}_{-0.69} \quad +0.26_{-0.20}$	$0.16^{+0.16}_{-0.14} \quad +0.01_{-0.00} \quad ‡$
Z_{Si}	$0.00^{+0.48}_{-0.00} \quad +0.19_{-0.00}$	—
Z_{Fe}	$0.27^{+0.06}_{-0.06} \quad +0.02_{-0.01}$	—
N^{\S}	$8.9^{+0.5}_{-0.5} \quad +0.0_{-0.0} \times 10^{-2}$	$7.4^{+0.6}_{-0.5} \quad +1.2_{-1.6} \times 10^{-2}$
$\chi^2/\text{d.o.f.}$	232.1/218	120.5/89

* Fitted to the XIS+PIN combined spectra.

† Fitted only to the XIS spectra.

‡ In the fitting to the NWR data, all abundances are linked together.

§ Normalization in apec model. Note that it is normalized to the whole cluster, not within the observation FOV, using the arf files generated from the PSPC image.

the emission from the cluster center. The XIS and the PIN spectra, therefore, not necessarily show the same result, although they should be roughly consistent with one another as a whole.

The XIS spectra of the 17' offset pointing can be represented using the $1kT$ model, with $kT = 7.6_{-0.4}^{+0.5}$ keV and $\chi^2/\text{d.o.f.} = 220.3/206$. Note that we utilized the arf files generated in section 2.4 so that the (energy dependent) vignetting effect is fully taken into account. For the same reason, the fitted flux is normalized to the reference image used in the arf generation (in this case the whole cluster), not just the flux within the FOV. When we use the XIS+PIN combined spectra, the $1kT$ model is acceptable as well, with a null-hypothesis probability of 24.5%. Results of the fitting are presented in table 5. As shown in figure 6 (a), however, the model slightly under-predicts the data in the PIN band. The residual resides right on the 90% upper-limit of the CXB and NXB systematic error.

The 17' offset data is also consistent with the $2kT$ picture of the center pointing. In fact, when we applied the $2kT$ best fit model of the center pointing to the XIS-PIN spectra, a marginally acceptable fit was obtained by shifting its global normalization only by -1% (see also panel (b) of figure 6). The fit gives $\chi^2/\text{d.o.f.} = 270.3/222$ or a null-hypothesis probability of 1.5%. What is more, the PIN spectra is very well reproduced using the nominal CXB and NXB model.

In both the XIS and PIN spectra of the NWR pointing, the CXB and NXB systematic errors are not negligible, as shown in the panel (c) of figure 6. Here, we used the southern 1/3 region of the NWR pointing in the XIS analysis (hereafter 1/3 NW-south region) because it covers most of the radio relic and the other two regions have almost no signals. We restrict our fitting to the energy band from 0.7–7.5 keV and 0.7–6.0 keV in the XIS-FI and BI spectra, respectively. We first applied the $1kT$ model to the XIS spectra. The best-fit temperature thus obtained is as low as $3.6_{-0.7}^{+0.6}$ keV (see table 5), which is significantly cooler than those of the center and 17' offset data. The fit is marginally acceptable with a null-hypothesis probability of 1.5%. Noticeably large residuals appears around 0.9 keV suggesting an additional ~ 1 keV thermal emission component. The XIS data is further analyzed in section 3.4.3.

The NWR PIN signal (shown in the panel (c) of figure 6) could be explained by the CXB and NXB systematic errors, since the level is right on their 90% confidence upper-limit. Another reasonable possibility is the ICM contribution from the cluster central region to the PIN spectra. Based on the arf files derived in section 2.4, 37% and 49% of the ICM contribution to the NWR-PIN data is originated from within 13' and 26' from the cluster X-ray centroid, respectively, which correspond to the area of the center and 17' offset XIS FOVs. In other words, only 14% is estimated to come from the cluster periphery, i.e. $> 26'$ from the cluster center. As shown later in section 3.4.1, the ICM contribution estimated using the XIS can explain all of the PIN signals in the NWR pointing. As a cross check, we also introduce the *XMM* mosaic data (e.g. Briel et al. 2004) covering the entire PIN FOV later in section 3.4.2, and come to the same conclusion.

Table 6. Spectral parameters of the power-law model fitted to the HXD spectra of the 17' offset and the NWR pointings in the 13–40 keV range.

Pointings	Γ	flux*	$\chi^2/\text{d.o.f.}$
17' offset	$3.5^{+1.2}_{-1.0} \text{ } ^{+0.9}_{-0.6}$	$19^{+4}_{-4} \text{ } ^{+6}_{-6}$	8.4/10
NWR	$3.4^{+2.0}_{-1.5} \text{ } \text{N/A}^\dagger$	$5.0^{+1.7}_{-1.7} \text{ } ^{+6.7}_{-5.0}$	7.5/10

* 10-40 keV flux of the power-law component, in $10^{-12} \text{ erg s}^{-1} \text{ cm}^{-2}$.

† N/A means the value was not available. In this case, the lack of photon made it impossible to restrict the spectral shape.

In table 6, we present the PIN spectral properties separately fitted to the 17' offset and the NWR data. Using the power-law model, the photon index Γ becomes as soft as 3.5. Although the error is large, the best-fit value is consistent with those obtained from the center PIN spectra (see table 3), while the flux itself is much brighter there. These results strongly suggest that the same emission dominant in the center-PIN spectra is contaminating both the 17' offset and the NWR PIN data.

3.3. Joint fit to the wide-band spectra of the three pointings

The PIN data of the three pointings are all mixed to some extent, mostly contaminated from the emission around the cluster center. In this section, we combine them to obtain the cluster overall properties.

Analysis of the three pointings suggests that all the data are consistent with the two component picture strongly suggested in the center pointing data, except for the XIS data in the NWR pointing showing rather low ICM temperature. Because of its low surface brightness, thermal contribution from this region is minor in the PIN band. Thus, we conducted a spectral analysis to the data combining in total 5 data sets (hereafter all-combined data), i.e. three PIN spectra and the XIS spectra of the center and 17' offset pointings.

As was the case with the center pointing, the $1kT$ model fitting to the all-combined spectra was unsuccessful, giving $\chi^2/\text{d.o.f.} = 1421.1/1248$ or a null-hypothesis probability of 4×10^{-4} . Thus, we applied the $2kT$ model to the all-combined spectra. Here the normalization ratios to the center XIS-FI spectra were set free in the XIS spectra of 17' offset data, while those of all PIN data were fixed at unity.

The $2kT$ fit was almost acceptable as shown in figure 7 and table 7. The null-hypothesis probability of the fitting was 8.1%. Partly because of the slight discrepancy of the spectral shape around 1 keV between the center and the 17' offset pointings, the hotter component temperature was not determined well when the NXB and the CXB systematic errors were included in the fit. However, the best-fit value of the hotter component temperature kT_{hi} is still 14.6 keV, which is consistent with the results from the center pointing data (see section 3.1.3).

The $1kT + PL$ model fitting to the all-combined spectra gave results similar to those of the center pointing (table 7). The fit itself was marginally acceptable with a null-hypothesis

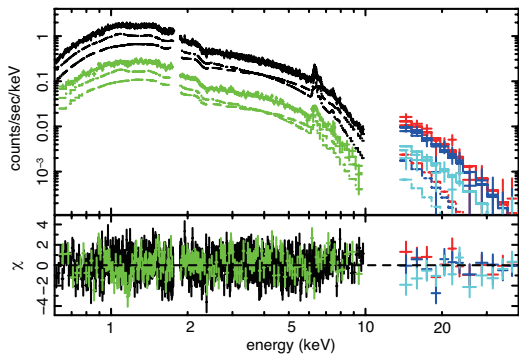


Fig. 7. The all-combined spectra fitted with the $2kT$ model. For simplicity, the XIS-BI spectra are not shown, although used in the actual fitting. The XIS and the PIN spectra of the center pointing are shown with black and red crosses, respectively, and those of the $17'$ offset pointing are shown with green and blue, as well. Crosses in light-blue give the PIN spectrum of the NWR pointing.

Table 7. Best fit parameters of the $2kT$ model and $1kT + PL$ model fitted to the all-combined spectra. Columns are similar to those presented in table 4.

	$2kT$	$1kT + PL$
kT_{lo}	$4.74^{+0.34}_{-0.67} \quad ^{+0.00}_{-2.74}$	$6.38^{+0.16}_{-0.15} \quad ^{+0.34}_{-0.42}$
kT_{hi}	$14.6^{+2.6}_{-3.4} \quad ^{+9.9}_{-7.1}$	–
Z_O	$0.49^{+0.17}_{-0.16} \quad ^{+0.00}_{-0.19}$	$0.50^{+0.19}_{-0.19} \quad ^{+0.00}_{-0.00}$
Z_{Si}	$0.28^{+0.11}_{-0.11} \quad ^{+0.03}_{-0.00}$	$0.27^{+0.13}_{-0.13} \quad ^{+0.03}_{-0.03}$
Z_{Fe}	$0.38^{+0.02}_{-0.02} \quad ^{+0.00}_{-0.04}$	$0.34^{+0.02}_{-0.02} \quad ^{+0.02}_{-0.02}$
N_{lo}	$5.5^{+0.7}_{-1.5} \quad ^{+0.7}_{-0.0} \times 10^{-2}$	$8.4^{+0.4}_{-0.4} \quad ^{+0.7}_{-0.7} \times 10^{-2}$
N_{hi}	$4.0^{+1.4}_{-0.8} \quad ^{+4.8}_{-0.5} \times 10^{-2}$	–
Γ_{PL}	–	$1.42^{+0.12}_{-0.18} \quad ^{+0.00}_{-0.02}$
F_{PL}	–	$24.7^{+5.2}_{-5.0} \quad ^{+22.2}_{-21.6}$
$\chi^2/d.o.f.$	1316.5/1246	1361.0/1246

probability of 1.2%, significantly worse than that of the $2kT$ model fitting. Thus the all-combined fitting also prefers the $2kT$ picture.

From this combined spectral analysis, it is clear that the all-combined spectra are generally consistent with the two component picture required in the center pointing data. The NWR-PIN data is well explained by the contribution from the cluster central portions, suggesting there is no strong signal of the IC emission in the data.

3.4. Search for the IC signal from the north-west radio relic

The north-west radio relic region is mostly covered by the deep (81 ks in the XIS and 48 ks in the HXD) NWR pointing. Although there is no strong evidence for the IC emission in the analysis so far, there should be some X-ray and hard X-ray emission from the relic. In

Table 8. Event counts in the 13–40 keV NWR-PIN data, compared to various error components.

Components	counts s ⁻¹
Signal	$(12.4 \pm 4.8) \times 10^{-3}$
4.3% of NXB*	$\pm 13.4 \times 10^{-3}$
18% of CXB [†]	$\pm 4.6 \times 10^{-3}$
ICM _{2kT} [‡]	$(24.3 \pm 6.0 \pm 2.4) \times 10^{-3}$
ICM _{1kT} [‡]	$(14.9 \pm 2.1 \pm 1.5) \times 10^{-3}$
ICM _{XMM} [‡]	$(14.7 \pm 1.5 \pm 1.5) \times 10^{-3}$
Signal _{2kT} [§]	$(-11.9 \pm 4.8 \pm 15.6) \times 10^{-3}$
Signal _{1kT} [§]	$(-0.8 \pm 4.8 \pm 14.4) \times 10^{-3}$
Signal _{XMM} [§]	$(-0.6 \pm 4.8 \pm 14.3) \times 10^{-3}$
$F_{2kT \text{ PL}}^{\#}$	$-4.6 \pm 1.8 \pm 6.0$
$F_{1kT \text{ PL}}^{\#}$	$-0.3 \pm 1.8 \pm 5.5$
$F_{XMM \text{ PL}}^{\#}$	$-0.2 \pm 1.8 \pm 5.5$

* Estimated NXB systematic error at the 90% confidence.

[†] Estimated CXB fluctuations at the 90% confidence.

[‡] ICM emission component estimated using the $2kT$ model fitted to the center XIS-PIN combined data, the $1kT$ model fitted to the 17' offset XIS data, and to the *XMM* weighted data. Values are shown with 90% fitting error including the NXB+CXB systematic effect in quadrature sum and 10% arf calibration systematic error.

[§] Non-thermal signals in counts s⁻¹ with 90% statistical and systematic errors. The latter value is the quadrature sum of those associated with NXB, CXB and the ICM.

[#] The 10–40 keV band flux in 10⁻¹² erg s⁻¹ cm⁻² derived from the “Signal” column, converted to a $\Gamma = 2.1$ power law emission.

this section, we focused mainly on this region to detect or determine the upper-limit on the IC emission.

3.4.1. The HXD upper limit combined with the XIS results

We evaluated the flux of the possible non-thermal hard X-ray emission using the 13–40 keV PIN signal of the NWR pointing. In table 8, signal rates are summarized with their errors. To estimate the ICM components, we used both the $2kT$ model fitted to the center XIS-PIN combined spectra and the $1kT$ model fitted to the 17' offset XIS-only spectra. The 17' offset PIN data was not used, because it may contain some signal from the north-west radio relic.

Using the center- $2kT$ model, we converted the residual signal in the NWR-PIN data by assuming a $\Gamma = 2.1$ fixed power-law emission located at the FOV center. The result is $(-4.6 \pm 1.8 \pm 6.0) \times 10^{-12}$ erg s⁻¹ cm⁻², i.e. $< 1.7 \times 10^{-12}$ erg s⁻¹ cm⁻² in the 10–40 keV band. Here again, the CXB and the NXB systematic errors and the 10% systematic error in the arf files are taken into account. Note that the arf files are used to estimate the ICM contribution, but not in the hard excess flux evaluation. Using the $1kT$ model fitted to the 17' offset XIS

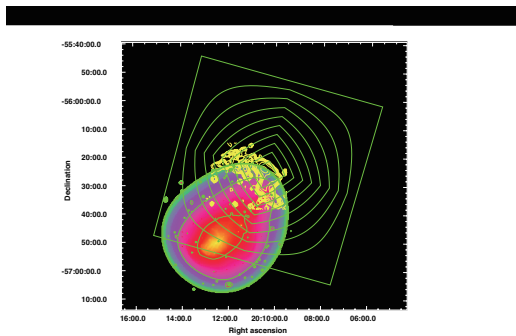


Fig. 8. The wavelet smoothed *XMM-Newton* mosaic image of Abell 3667 with a logarithmic color scale (Briel et al. 2004). The green square is the total FOV of the PIN for the NWR observation. The interior green regions are curves of constant PIN effective area, ranging from 10% to 90% of the effective area for a central point source. The yellow contours are from the SUMSS 842 MHz radio image of the NW radio relic. See text for detail.

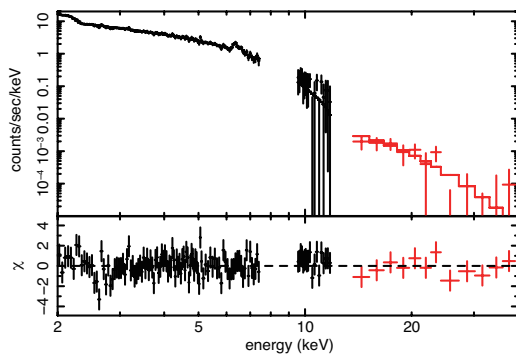


Fig. 9. The NWR-PIN spectra combined with the *XMM* spectra. The best-fit $1kT$ model is shown.

spectra, the power-law flux is estimated to be $(-0.3 \pm 1.8 \pm 5.5) \times 10^{-12} \text{ erg s}^{-1} \text{ cm}^{-2}$, i.e. $< 5.5 \times 10^{-12} \text{ erg s}^{-1} \text{ cm}^{-2}$ in the 10–40 keV band. Since the contribution from the central portion and 17' offset region are both significant, actual upper-limit on the power-law emission will be somewhere between these two values. Here, we recognize the latter results, $< 5.8 \times 10^{-12} \text{ erg s}^{-1} \text{ cm}^{-2}$, as the conservative upper-limit flux of the excess hard X-rays from the north-west relic.

Table 9. Best fit parameters of the $1kT$ model fitted to the *XMM*-pn spectra, weighted with the HXD-PIN vignetting function of the NWR pointing.

kT^*	Abun. [†]	$\chi^2/\text{d.o.f.}$
$7.93^{+0.43}_{-0.42}$	$0.22^{+0.04}_{-0.04}$	116.6/123

* Temperature of the apc model.

* Metal abundance of the apc model.

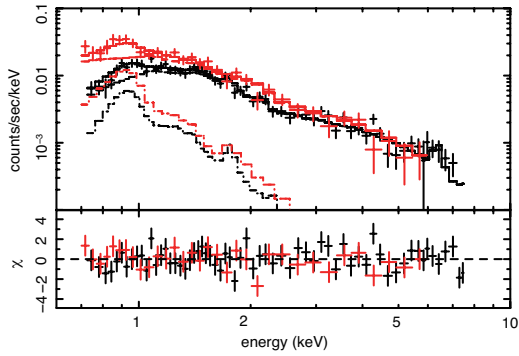


Fig. 10. The XIS spectra of the 1/3 NW-south region fitted with $2kT$ thermal model. Note the cool component at ~ 0.9 keV.

3.4.2. The HXD upper limit combined with the XMM results

Mapping observations performed by *XMM-Newton*, as described in Briel et al. (2004), provides independent information of the ICM and its temperature distribution. With its larger FOV, the *XMM* data has a merit on observing almost all of the ICM emission covered by the HXD-PIN FOV, while the XIS has the merit of low background and simpler cross-calibration with the HXD.

The *XMM* spectra, background and arf files for this analysis are generated using the method described in Wik et al. (2008). In summary, we defined 10 regions with nearly constant PIN effective area, separated by curves with 0%, 10%, 20%, ... 90% of the value for the central point source, as shown in figure 8. Then we extracted *XMM* EPIC-pn spectra from these region in the standard manner, using the *XMM*-mosaic data and adopting the XMMSAS v7.1 calibration. The background spectrum is derived from the datasets compiled by Read & Ponman (2003), and we also apply consistent flare cleaning criteria to both the data and the background. By adding the 10 signal spectra multiplied by the PIN vignetting function, and correcting the *XMM*-XIS cross normalization of 15%, we obtain the *XMM* spectra scaled to the same normalization as that of the NWR-PIN spectra. To avoid the contribution of the soft emission components to the results, we performed the spectral fitting above 2 keV, and also masked the energy-region in which the background lines (mostly from Ni) are prominent.

In figure 9, we present the *XMM*-pn spectra fitted with the $1kT$ model. Parameters are summarized in table 9. The NWR-PIN spectra is remarkably consistent with the *XMM*-best-fit model superposed, as also shown in the figure. Thus, using the *XMM*, we independently obtained a result that no additional hard X-ray component is required in the NWR-PIN data. As shown in table 8, the power-law flux is estimated to be $(-0.2 \pm 1.8 \pm 5.5) \times 10^{-12}$ erg s $^{-1}$ cm $^{-2}$, i.e. $< 5.6 \times 10^{-12}$ erg s $^{-1}$ cm $^{-2}$ in the 10–40 keV band.

3.4.3. The XIS image and spectral analysis

The 1/3 NW-south region of the NWR-XIS data covers most of the radio relic. Since its background is low and stable, the XIS data contains good informations on the IC emission

Table 10. Spectral parameters of the power-law model fitted to the 1/3 NW-south XIS spectra.

Γ	flux*	$\chi^2/\text{d.o.f.}$
$1.9^{+0.1}_{-0.1}$	$0.47^{+0.14}_{-0.11}$	56.2/45

* 10-40 keV flux of the power-law component, in 10^{-12} erg s $^{-1}$ cm $^{-2}$.

from the relic itself.

We first investigated the XIS spectral properties in detail. In the NWR region, the diffuse X-ray emission is weak and dimmer point sources can be identified easily. As shown in figure 1, we identified two sources with flux $1.5 \sim 3.5 \times 10^{-14}$ erg s $^{-1}$ cm $^{-2}$ in the 2–10 keV band, and masked out 2' around them. When we perform the same operation to the Lockman Hole observation, we found two sources as well. There the overall CXB level decreases by $\sim 10\%$ after masking these sources. This shift is fed back into the CXB estimation of the NWR analysis here. Since the upper cutoff flux is changed to $S_c \sim 2 \times 10^{-14}$ erg s $^{-1}$ cm $^{-2}$ from $\sim 1 \times 10^{-13}$ erg s $^{-1}$ cm $^{-2}$, the CXB fluctuation level is reduced to 12.7% from the original 19% (see appendix 1).

In figure 10, the XIS-FI and BI spectra of the 1/3 NW-south data obtained after masking the sources are shown. When fitted with a $1kT$ model, the fit is marginally acceptable, giving $\chi^2/\text{d.o.f.} = 125.4/92$ or 1.2% in null hypothesis probability. In this analysis, we used an arf file for a spatially flat emission, and scaled the result using the angular size to obtain the flux within the 1/3-NW south region. The temperature is 4.0 ± 0.7 keV, slightly higher than the value obtained in section 3.2, but well within its errors. To handle the significant hump at around 0.9 keV, we added another thermal component (the $2kT$ model). Then we obtained an acceptable fit with $\chi^2/\text{d.o.f.} = 90.8/90$. The hot component temperature is derived as $kT_{\text{hi}} = 5.4^{+1.7}_{-1.4}$ keV and that of the cool one as $kT_{\text{lo}} = 0.94^{+0.16}_{-0.18}$ keV, while the common abundance is $0.37^{+0.32}_{-0.23}$ solar. The significance of the Fe-K lines is weak, with a probability of 13% by the f -test, which is not surprising considering the low surface brightness. Since the flux of the cool component at ~ 0.9 keV is similar to that of the CXB model, the emission could be either a slight hump in the “foreground Galactic component” or some cool component really associated with the cluster periphery.

Since the region coincides in position with the diffuse radio emission, the detected X-rays might be of non-thermal origin. As an extreme case, we fit the spectra with a power-law model. Because of the 0.9 keV hump, which indicates a contribution from $kT \sim 1$ keV thermal component, we utilized the energy band above 1.5 keV in this fitting. We also limit it to below 6.0 keV since the NXB systematic error dominates above this energy. The results are listed in table 10. The power-law fit is acceptable with a null-hypothesis probability of 12%. Taking into account the large systematic errors associated with the NXB and CXB (see figure 6c), we cannot distinguish whether the emission is thermal or non-thermal from spectroscopy only.

In figure 11, we present the projected X-ray count-rate map in the energy bands of 1–2 keV, 2–4 keV and 4–8 keV derived from all the three XIS-FI detectors. Here, the BI chip is not utilized because of its higher background. Regions around the two point source in the NWR data are excluded in the plot. Overlaid is the profile of the SUMSS 843 MHz radio image, which clearly shows the relic, located $\sim 30'$ (2 Mpc) away from the X-ray centroid. From the 1–2 keV and 2–4 keV profiles, it is clear that the cluster emission was detected out to the region $40'$ from the cluster center, which corresponds to 2.6 Mpc in projected distance. On the other hand, there is apparently no excess signal associated with the radio relic, smoothly connecting the inner ICM X-rays to the CXB component at the outermost region. Thus, a significant fraction of the X-rays in the NWR region was naturally assumed to be of thermal origin.

Using this plot, we roughly evaluated the upper-limit of the projected non-thermal count rates associated with the relic. Here, we assumed that the IC emission has the same morphology to that of the radio emission, and the 2–8 keV X-ray counts within region B in figure 11 are the upper-limit to the IC emission. The CXB is estimated from region C, and its fluctuation is calculated to be 22% on both the region A and B. Taking the statistical error and the CXB fluctuation into account, relative count-rate of region B to that of region A is derived as $0.48_{-0.17}^{+0.22}$ while that of the radio flux is 1.17. Thus, we concluded that $40_{-16}^{+16}\%$, i.e. larger than 24%, of the emission in region A+B is of thermal origin. Since the region A+B almost coincides with the 1/3 NW-south region, we combine this result with the power-law fitting results (table 10). In addition, because the radio emission within the spectral fitting region only covers 78% of the total relic flux in the SUMSS image, we multiply the XIS flux by a factor of 1.3 to match them. Finally, we obtain the 10–40 keV upper limit IC flux for the north-west radio relic as a whole as $6.8 \times 10^{-13} \text{ erg s}^{-1} \text{ cm}^{-2}$ allowing Γ to vary, at the 90% confidence level. With this flux, the photon index is required to be $\Gamma = 1.6$. If we fix it to $\Gamma = 2.1$, the 10–40 keV upper limit flux become $3.5 \times 10^{-13} \text{ erg s}^{-1} \text{ cm}^{-2}$.

4. Discussion

4.1. Short summary of the analysis results

We analyzed the *Suzaku* mapping observation data of a merging cluster Abell 3667. The XIS detects emission from the cluster out to $\sim 40'$ or 2.6 Mpc from the cluster center. The PIN spectra of the three pointings commonly prefer soft-shaped spectra, suggesting that the thermal contribution from the cluster ICM is the major origin of these signals. From the XIS+PIN combined analysis of the center pointing, the two-phase thermal picture of the $2kT$ model (or the $1kT + PL$ model) is suggested. In the former case, kT_{hi} is derived to exceed 12.9 keV, with the best fit value around 20 keV, while kT_{lo} is around 4.7 keV. This result suggests the existence of very hot (~ 20 keV) component around the cluster center.

The XIS spectra of the $17'$ offset pointing can be fitted using the $1kT$ model with $kT \sim 8$

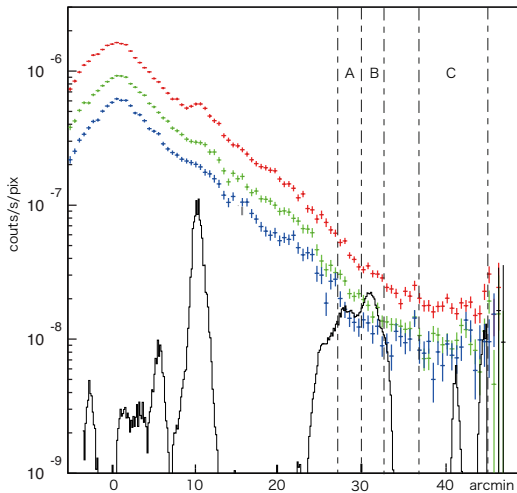


Fig. 11. Projected X-ray image in the energy band of 1–2 keV, 2–4 keV and 4–8 keV in red, green and blue crosses, respectively. The width of the projection region is $12'$ along the merger axis, as shown in figure 1. Black histogram stands for SUMSS 843 MHz radio image obtained via Skyview service by NASA, projected in the same manner but with arbitrary normalization. The region A, B and C are those used for IC upper-limit analysis. See text for detail.

keV, while that of the southern one third of the NWR pointing (the $1/3$ NW-south region) requires a cooler value, around 4 keV. The PIN signal in the NWR pointing can be explained by the ICM contribution with either the $2kT$ picture suggested by the center pointing or the $1kT$ picture fitted to the $17'$ offset XIS data. The shape of the PIN spectra of the center and $17'$ offset pointings are too soft to account for the $\Gamma = 2.1$ IC emission suggested from the radio observation. Thus, the wide-band *Suzaku* X-ray spectra do not show any signature of the IC emission associated with the strong (3.7 Jy at 1.4 GHz) radio synchrotron emission.

Using the HXD, the overall upper-limit 10–40 keV flux on the non-thermal emission within a $34' \times 34'$ FOV around the north-west radio relic is derived to be 5.5×10^{-12} erg s^{-1} cm^{-2} with the $1kT$ ICM modeling. The ICM modeling using the *XMM*-pn spectra gives a similar upper limit. Using the XIS, the upper-limit on the radio relic itself is derived to be 3.5×10^{-13} erg s^{-1} cm^{-2} , when converted into the 10–40 keV band and assuming $\Gamma = 2.1$. If we allow the index to be free, i.e. assume that there is a spectral break somewhere above 10 keV, the upper-limit value became 6.8×10^{-13} erg s^{-1} cm^{-2} .

4.2. The magnetic field in the north-west radio relic

By combining the radio and X-ray observations, here we estimate the magnetic field strength in the north-west radio relic. From the radio observation, the relic has a flux of 3.7 Jy at 1.4 GHz (Johnston-Hollit 2008). Its radio fluxes at 85 MHz, 843 MHz, 1.4 GHz and 2.3 GHz are reported to roughly follow the power law with $\Gamma = 2.1$ (Roettgering et al. 1997). With a magnetic field of $1 \mu\text{G}$, the 85 MHz radio emission requires electrons with a Lorentz factor γ of $\sim 5 \times 10^3$, which in turn emits IC photon at around 20 keV. In the case of 1.4 GHz radio

emission, they are $\gamma \sim 2 \times 10^4$ and 350 keV, respectively. Thus, we will assume that the photon index is similar to $\Gamma = 2.1$ above 20 keV, when the magnetic field is stronger than $1 \mu\text{G}$.

The radio flux at the 80–320 MHz band, which corresponds to the ~ 20 keV IC emission with $B = 1 \mu\text{G}$, is derived as $F_{80-320 \text{ MHz}}^{\text{Sync}} = 1.8 \times 10^{-13} \text{ erg s}^{-1} \text{ cm}^{-2}$, assuming a $\Gamma = 2.1$ power-law emission and a flux of 3.7 Jy at 1.4 GHz. The XIS upper-limit right on the north-west radio relic region is derived as $F_{10-40 \text{ keV}}^{\text{IC}} < 3.5 \times 10^{-13} \text{ erg s}^{-1} \text{ cm}^{-2}$, again assuming a simple $\Gamma = 2.1$ power law. By dividing these two values, we obtain

$$\begin{aligned} \frac{F^{\text{Sync}}}{F^{\text{IC}}} &= \frac{U_{\text{B}}}{U_{\text{CMB}}} \\ &= \left(\frac{B}{B_{eq.}^{\text{CMB}}}\right)^2 > \frac{1.8 \times 10^{-13}}{3.5 \times 10^{-13}}. \end{aligned}$$

Here, $B_{eq.}^{\text{CMB}} = 3.2 \mu\text{G}$ is the equivalent magnetic field of the energy density of the CMB. Thus, the magnetic field in the north-west radio relic is inferred to be $B > 2.3 \mu\text{G}$.

Since the radio emission is detected only down to 85 MHz, the IC spectra below ~ 20 keV might have a break. For the electrons with $\gamma = 5 \times 10^3$ within a thermal gas density of $\sim 1.3 \times 10^{-4} \text{ cm}^{-3}$ (derived from the XIS results), the dominant cooling processes are the IC and the synchrotron emissions. These give a cooling time of $\sim 4 \times 10^8$ years. If the duration of electron injection is shorter than this time-scale, the electron distribution below this energy is not affected by the cooling, and the resultant IC (and synchrotron) photon index can be harder, typically $1.5 < \Gamma < 2.1$. From the Γ free power-law fitting to the 1/3 NW-south spectra of the XIS, we know that the upper-limit IC flux in the 10–40 keV band is $6.8 \times 10^{-13} \text{ erg s}^{-1} \text{ cm}^{-2}$. In this model, the photon index is 1.6 around 4 keV, and breaks to 2.1 above ~ 20 keV. In this case, the magnetic field strength is inferred to be $B > 1.6 \mu\text{G}$. These results are consistent with the radio rotation measure observations of this relic, suggesting 3–5 μG (Johnston-Hollitt 2004).

Based on the observable parameters, we calculate the energy density of individual components in the north-west radio relic. The thermal particle density and temperature give an energy density U_{th} of 1.0 eV cm^{-3} . Here, we simply assume that all X-rays in the north-west relic are of thermal origin. With a magnetic field strength of $> 2.3 \mu\text{G}$ and $> 1.6 \mu\text{G}$, the energy density U_{B} is derived as $> 0.13 \text{ eV cm}^{-3}$ or $> 0.07 \text{ eV cm}^{-3}$, respectively. Here, on the contrary, we assume that most of the X-rays are of IC origin to give an upper limit on U_e . If a power-law distribution of relativistic electrons are assumed within $5 \times 10^2 < \gamma < 4 \times 10^4$, the energy density of electrons U_e is $< 0.14 \text{ eV cm}^{-3}$. Here the minimum γ is assumed to be the critical Lorentz factor below where ionization losses dominate (Sarazin 1999). Although U_e strongly depends on the unknown electron distribution below $\gamma \sim 5 \times 10^3$, the calculated upper-limit value is not so far from the equi-partition condition.

The ratio between the thermal (U_{th}) and non-thermal energy density (U_{B} and U_e) is inferred to be as large as 20%. Although U_e has a large uncertainty, the lower limit on U_{B} is

much more robust. In addition, $U_B/U_{\text{th}} > 0.07$ is a strong limit. If we assume, for example, that about a half of the X-rays in the north-west relic are of thermal origin and the latter half is of IC origin, U_{th} is decreased by a factor of $\sqrt{2}$ and the lower limit on the U_B is doubled. In this case, the ratio becomes as high as 19%, excluding the U_e contribution. Our results are generally consistent with those by Rottgering et al. (1997), though they do not discuss in detail the magnetic field.

This demonstrates that magnetic fields stronger than $1 \mu\text{G}$ exist on scales as large as the cluster virial radius and exert non-negligible pressure compared to the thermal one, at least around the region of the north-west relic. Recent observations of radio relics around other clusters have also revealed similarly strong magnetic fields of $> 0.8 \mu\text{G}$ (e.g. Feretti & Neumann 2006; Henriksen & Mushotzky 2001; Hubert et al. 2008). That of the Abell 3667 north-west relic is the strongest yet observed.

It is important to note that the large magnetic field we have found applies only to the interior of the radio relic. Thus, it is possible that most clusters do not have such large fields at such outer radii. The relic is the brightest diffuse cluster radio source known, and its interior may not be typical of the diffuse intracluster medium outside the relic, or in other clusters. It may be that the magnetic field and seed relativistic particles were injected into this region by an AGN in the past (e.g. Ensslin & Gopal-Krishna 2001). If the relativistic electrons were accelerated by a merger shock, the same shock may have amplified the magnetic field, perhaps by some mechanism like the Weibel instability (e.g. Okabe & Hattori 2003; Kato 2007; Fujita et al. 2006) or the cosmic ray streaming instability (Lucek & Bell 2000, Bell 2004). Also, Abell 3667 has undergone a very dramatic merger, and may not be typical of more relaxed clusters.

4.3. Implications of the upper-limit of the IC emission using the HXD-PIN

The HXD-PIN data of the NWR pointing provides an upper-limit on the IC emission as $5.5 \times 10^{-12} \text{ erg s}^{-1} \text{ cm}^{-2}$. Since the FOV of the PIN is ~ 10 times larger than the region used in the XIS analysis, it provides valuable limits on any non-thermal electrons that may be distributed on scales larger than the north-west relic. These electrons, in addition, are not readily observable in the radio band. For example, if the relic is surrounded by a larger region with lower magnetic field, say $0.3 \mu\text{G}$, electrons therein with $\gamma \sim 5 \times 10^3$ would be unobservable through their synchrotron emission since its frequency is less than 10 MHz.

Using the *Beppo-SAX* PDS data with an equivalent exposure (113 ks) to the NWR pointing, Fusco-Femiano et al. (2001) derived the upper-limit hard X-ray flux of $\sim 6.4 \times 10^{-12} \text{ erg s}^{-1} \text{ cm}^{-2}$ in the 20–80 keV band assuming a $\Gamma = 2.1$ power-law emission. Here, they fixed the ICM temperature to 7 keV and included only the statistical errors. Using the same data with similar thermal model, Nevalainen et al. (2004) presented a 90% confidence upper limit flux of $7.1 \times 10^{-12} \text{ erg s}^{-1} \text{ cm}^{-2}$ in the same energy band assuming a power-law with $\Gamma = 2.0$. The main

difference in the two results is that the latter author took into account the possible systematics in the PDS background modeling and AGN contribution derived in their own manner.

By comparing the observational results on the Crab, we found that the 20–80 keV flux derived from *Beppo-SAX* PDS is 21% smaller than those derived from *Suzaku*. Thus, results from Fusco-Femiano et al. (2001) and Nevalainen et al. (2004) can be converted into *Suzaku*-equivalent fluxes of 8.1 and 9.0×10^{-12} erg s⁻¹ cm⁻², respectively. Therefore, our *Suzaku* result provides more stringent upper limit on the flux, compared to these two results. Furthermore, it is focused on a more spatially restricted region around the north-west radio relic, thanks to the narrow FOV of the HXD ($\phi \sim 34'$ FWHM) compared to that of the PDS ($\phi \sim 1.3^\circ$ FWHM).

4.4. Possible very hot component in the merging cluster

The HXD-PIN results from the cluster center shows a “soft-shaped” hard component with $\Gamma = 3.6_{-0.9}^{+1.1}$, which can be best interpreted as a very hot component with a temperature of $18.5_{-5.6}^{+6.8}$ keV, in addition to the ~ 4.7 keV component. Since the spectra can be marginally fitted with a $\Gamma \sim 1.4$ power-law component, the emission could be of non-thermal origin, or contamination from a yet unknown Compton-thick AGN. However, our contaminating point-source survey (appendix 3) and the softness of the spectral shape itself suggests the thermal interpretation. The excess signal to the $1kT$ component is significant in the center pointing, and consistent with the two offset pointings as well. Thus the very hot component can be significant around the cluster center.

From the *ASCA* observations, this cluster is known to host significant temperature inhomogeneity, showing regions with a temperature as high as 10 keV together with the 4–6 keV dominant emission (Markevitch 1998). Later, Briel, Finoguenov & Henry (2004) also showed the complex multi temperature nature of the ICM using the *XMM* data. The temperature ranges from 4 keV to 8 keV, and several hot regions are visible around the cluster center. Since these analyses are based on the projected X-ray color maps, the temperature of the actual hottest component can be higher considering the convolution along the line-of-sight. The *Beppo-SAX* PDS spectrum is consistent with the center- $2kT$ model taking into account all the systematics. Thus, our results on “soft-shaped” hard component is basically consistent with existing data.

Such a very hot component, with a temperature as high as 20 keV, is suggested by many hydrodynamical simulations of merging clusters right after the time of impact (e.g. Takizawa 2000). Since the Abell 3667 cluster is considered to be at this stage, the very hot component will be the hottest heated ICM emission. We note that a similar very hot component is suggested in the cluster RXJ1347.5–1145 (Ota et al. 2008) using the *Suzaku* wide-band data combined with *Chandra* spectra. Its high temperature and relatively large luminosity means that the very hot component cannot be in pressure balance with the cooler one, otherwise, it will dominate the volume in the cluster. Thus, the emission should be temporary originating from the shock and/or the compression heating, and is expected to disappear soon by adiabatic expansion. To

investigate the location of the emission, we will need much wider energy band coverage in the imaging detector, specifically, arcmin-scale imaging spectroscopy up to ~ 40 keV.

5. Conclusion

From *Suzaku* mapping observations of Abell 3667, upper-limits on the non-thermal (hard) X-ray emission were obtained. On the north-west radio relic itself, the XIS limit of 6.8×10^{-13} erg s $^{-1}$ cm $^{-2}$ extrapolated to the 10–40 keV band provides a lower-limit magnetic field of > 1.6 μ G. The non-thermal energy density there is estimated to be higher than 7%, and likely near 20%.

By combining the XIS and the *XMM* mapping data to the HXD-PIN spectra, the upper limit on the 10–40 keV excess hard emission is derived as $1.7\text{--}5.5 \times 10^{-12}$ erg s $^{-1}$ cm $^{-2}$, depending on the modeling of the ICM. Since the north-west relic has a magnetic field of > 1 μ G and hence must be almost an order of magnitude darker than this hard X-ray limit, the relativistic electrons must be distributed in regions other than the relic with low magnetic field (of $B < 0.3$ μ G) if IC hard X-ray emission near the flux limit exists.

The PIN data from the pointing on the cluster center shows hard X-rays in excess to the averaged ICM emission, which is thought to have a temperature of around 7 keV. Although other interpretations cannot be rejected, its soft spectral shape indicates the emission to be possibly from a very hot thermal component with a temperature of ~ 20 keV, generated temporary in the cluster merger phase.

In the near future, X-ray observatories with hard X-ray imaging optics operating up to 40 keV will be launched, such as the ASTRO-H (former NeXT; e.g. Takahashi et al 2006), NuSTAR and Simbol-X (e.g. Ferrando et al. 2006). These detectors will drastically improve the sensitivity to both point sources and relatively clumpy extended hard X-rays, such as the local non-thermal emission associated with the radio halos/relics and the very hot component. In addition, the Soft Gamma-ray Detector onboard ASTRO-H, (a collimated instrument) features the highest sensitivity at around 100 keV using the novel narrow-field-of-view Compton camera concept. It will open a new window to the widely distributed non-thermal emission, which is difficult to separate from the ICM thermal emission below ~ 50 keV.

K.N. and K.M. are supported in part by a Grant-in-Aid from the Ministry of Education, Science, Sports, and Culture of Japan (18104004), and M.T. (16740105,19740096) and S.I (19047004, 19540283), as well. C.L.S. and D.R.W. were supported by NASA *Suzaku* grants NNX06AI44G and NNX06AI37G and *XMM-Newton* grant NNX06AE76G. D.R.W. was also supported by a Dupont Fellowship and a Virginia Space Grant Consortium Fellowship. A.F. was partially supported by NASA grant NNG05GM5OG to UMBC. Basic research in radio astronomy of T.C. at the NRL is supported by 6.1 Base funding.

Appendix 1. The CXB estimation for the XIS

The Lockman Hole observation (*Suzaku* observation ID, 101002010) was used as the CXB template. The NXB subtracted data from the Lockman Hole were fitted with a model composed of a power-law with a fixed Γ of 1.4, and thermal components (so called “Galactic components”) with one of the temperatures fixed at 0.08 keV and another fitted to give ~ 0.3 keV. The 2–10 keV flux of the power-law component was derived as $5.7 \pm 0.1 \times 10^{-8}$ erg s $^{-1}$ cm $^{-2}$ str $^{-1}$, which is consistent within 1σ from the best fit value derived using *ASCA* (Kushino et al. 2002).

We also analyzed the XIS data of the outer boundary for Abell 3667, using the northern 1/3 region of the NWR pointing (hereafter the 1/3 NW-north region). It gave a $\sim 16\%$ higher normalization for the power-law component, which is consistent with the expected fluctuation of CXB, discussed later in this section. The “Galactic component” parameters are similar, but the flux is brighter by a factor of 2–5, which is also consistent with its sky fluctuations. Because the 1/3 NW-north region could be contaminated by the outskirts of the cluster ICM emission, we modeled the CXB with the power-law component fixed at the value obtained from the Lockman Hole observation, while the “Galactic component” was fixed at that of the 1/3 NW-north region.

The CXB fluctuations can be modeled as $\sigma_{\text{CXB}}/I_{\text{CXB}} \propto \Omega_e^{-0.5} S_c^{0.25}$. Here, Ω_e is the effective solid angle and S_c is the upper cutoff flux. From the HEAO-1 A2 results, Shafer (1983) derived $\sigma_{\text{CXB}}/I_{\text{CXB}} = 2.8\%$, with $\Omega_e = 15.8$ deg 2 and $S_c = 8 \times 10^{-11}$ erg s $^{-1}$ cm $^{-2}$. By scaling this result with the XIS parameters, i.e. $\Omega_e = 0.09$ deg 2 and $S_c \sim 1 \times 10^{-13}$ erg s $^{-1}$ cm $^{-2}$ in the cluster vicinity, we obtain the CXB fluctuation over the XIS full FOV as 11% (90% confidence level). For the NWR 1/3 NW-north region (and the 1/3 NW-south region, as well), the value is then 19% when the S_c is unchanged. With $S_c \sim 2 \times 10^{-14}$ erg s $^{-1}$ cm $^{-2}$, it becomes 12.7%. Note that this scaling relation is consistent with the *ASCA* and *Ginga* CXB analysis (Ishisaki 1997).

Appendix 2. The CXB estimation for the HXD

The CXB flux in the PIN is modeled as a cutoff power-law, described as $N(E) = n \times (E)^{-\Gamma} \times \exp(-E/E_{\text{fold}})$ in photons cm $^{-2}$ s $^{-1}$ keV $^{-1}$ FOV $^{-1}$. Here, E_{fold} is an folding energy, and n is the normalization. In energies below ~ 80 keV, the HXD energy response for a diffuse source is the same to that for a point source except for its normalization. Thus, we simply scaled our CXB model to the solid angle of the HXD, $\Omega_e^{\text{HXD}} = 0.32$ deg 2 and utilized the HXD nominal response. We first used the parameters based on the HEAO-1 results (Boldt 1987), which gave $\Gamma = 1.29$, $E_{\text{fold}} = 40.0$ and $n = 8.36 \times 10^{-4}$. We then compared this model to the XIS observation of Lockman Hole, on which our XIS CXB modeling is based on. It was found that the model predicts a flux 8.6% lower in the XIS 3-8 keV band data. Thus, we modified the

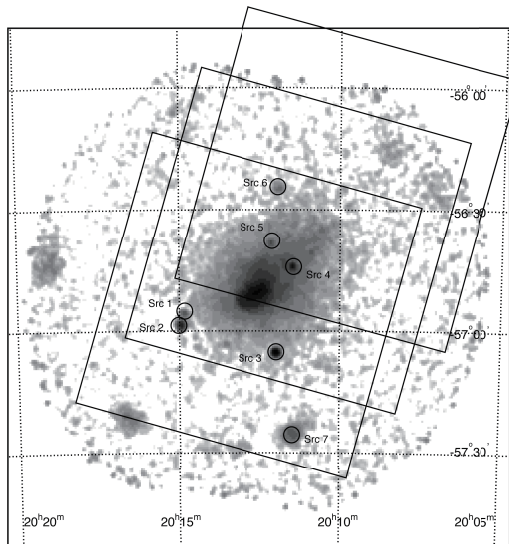


Fig. 12. The background subtracted *ROSAT* PSPC image (50' radius) of Abell 3667. Gray-scale contour is logarithmic scale. The FOVs (68' \times 68' bottom to bottom) of PIN are shown in thin rectangles, and X-ray point sources in the FOVs are shown in circles.

PIN CXB model normalization to match the difference, as $n = 8.69 \times 10^{-6}$. Note that although there is an apparent difference in photon index between the CXB model of the XIS and PIN, the cutoff function in the later makes two models perfectly matched in the energy band at 3–8 keV. Through the same approach applied to the XIS data, the CXB fluctuation in the HXD FOV is expected to be 18%, with $\Omega_e^{\text{HXD}} = 0.32 \text{ deg}^2$ and a conservative upper cutoff flux of $S_c \sim 8 \times 10^{-12} \text{ erg s}^{-1} \text{ cm}^{-2}$ in the 10–40 keV band.

Appendix 3. Estimation of point source contamination in the FOV of the PIN

Since the PIN has a wide FOV (68' \times 68' bottom to bottom) than that of the XIS (18' \times 18') and also lacks imaging capability, signal contamination from point sources within the FOV should be carefully estimated. Figure 12 shows the PSPC image of Abell 3667 with the FOVs of the PIN superposed. The PSPC data is processed through the method described by Snowden et al. (1994). There exists seven X-ray point sources in the PIN FOVs. We identified these sources using the SIMBAD astronomical database.

Source 4 and Source 6 are in the FOV of XIS, and thus their flux is estimated by the XIS data. Although the other sources are outside the FOV of XIS, archival data of *ASCA* GIS are available for the sources 1, 2, 3, and 5. We therefore extracted the GIS spectra of source 1 through source 6 and fitted them with a power law modified by galactic absorption. Blank sky observations of the GIS were used for the background of source 1, 2 and 3, while neighboring field is used for source 5.

Using the best-fit parameters, we simulated the PIN spectra of the six sources for the three pointings, considering the PIN transmission to each of them on the three pointings. The

total contribution of the six point sources thus estimated is more than an order of magnitude lower than the detected signal, and hence negligible. Source 7, not included in this estimation, is located at the boundary of the PIN FOV of the center pointing. It is also a weak hard X-ray source, since it is a distant cluster of galaxies.

References

- Anders E., & Grevesse N. 1989, *Geochim. Cosmochim. Acta*, 53, 197
- Bell A. R. 2004 *MNRAS* 353, 550
- Briel, U. G., Finoguenov, A., Henry, J. P., & Anders E., 2004, *A&A*, 426, 1
- Boldt E. 1987, *IAU Circ.*124, 611
- Carilli C. L. & Taylor G. B., 2002 *ARA&A*, 40, 319
- Clarke T. E., Kronberg P. P. & Böhringer H. 2001, *ApJL*, 547, 111
- Dickey J. M. & Lockman F. J. 1990, *ARA&A*, 28, 215
- Ensslin, T. A. & Gopal-Krishna 2001 *A&A*, 366, 26
- Feretti L., Neumann D.M., 2006 *A&A*, 450, L21
- Ferrando P. et al. 2006, *SPIE proc.*, 6266
- Fujita Y., Kato T. N. & Okabe N. 2006, *Phys. Plasma* 13, 122901
- Fukazawa Y., Nakazawa K., Isobe N., Makishima K., Matsushita K., Ohashi T. & Kamae T. 2001 *ApJL*, 546, 87
- Fukazawa Y., Makishima K., & Ohashi T. 2004, *PASJ*, 56, 965
- Fukazawa Y. et al. 2008, submitted to *PASJ*
- Fusco-Femiano, R., dal Fiume D., Feretti L., Giovannini G., Grandi P., Matt G., Molendi S. & Santangelo A. 1999, *ApJL*, 513, 21
- Fusco-Femiano R., Dal Fiume D., Orlandini M., Brunetti G., Feretti L., & Giovannini G. 2001, *ApJ*, 552, L97
- Fusco-Femiano R., Landi R. & Orlandini M. 2007, *ApJ*, 654, L9
- Henriksen M. & Mushotzky R. 2001, *ApJ*, 553, 84
- Hubert C. M., Harris D. E., Harrison F. A. & Mao P. H. 2008, *MNRAS*, 383, 1259
- Inoue S., Aharonian F. A. & Sugiyama N. 2005, *ApJ*, 628, L9
- Ishisaki, Y. 1997, Ph.D. thesis, University of Tokyo
- Johnston-Hollitt M. 2004, in *Proc. The Riddle of Cooling Flows in Galaxies and Clusters of Galaxies*, ed. T. H. Reiprich, J.C. Kempner, & N. Soker, 51
- Johnston-Hollitt M., Hunstead R. W. & Corbett, E. 2008, *A&A*, 479, 1
- Kato T. N. 2007, *ApJ*, 668, 974
- Kitaguchi T. et al. 2008, submitted to *PASJ*
- Knopp G. P., Henry J. P., & Briel U. G., 1996, *ApJ*, 472, 125
- Kokubun M., et al. 2007, *PASJ*, 59, 53
- Koyama K., et al. 2007, *PASJ*, 59, 23
- Kushino A., Ishisaki Y., Morita U., Yamasaki N. Y., Ishida M., Ohashi T. & Ueda Y. 2002, *PASJ*, 54, 327

Lucek S. G. & Bell A. R. 2000 MNRAS314, 65
Markevitch M., Sarazin C. L., & Vikhlinin A. 1999, ApJ, 521, 526
Mazzotta P., Fusco-Femiano R., & Vikhlinin A. 2002, ApJ, 569, L31
Mitsuda K., et al. 2007, PASJ, 59, 1
Mohr J. J., Mathiesen B. & Evrard A. E. 1999, ApJ, 517, 627
Nakazawa K., Makishima K., & Fukazawa Y. 2007, PASJ, 59, 167
Nevalainen J., Oosterbroek T., Bonamente M., & Colafrancesco S., 2004, ApJ, 608, 166
Neumann D. M. & Arnaud M. 1999, A&A, 348, 711
Okabe N. & Hattori M. 2003, ApJ, 599, 964
Ota N., Murase K., Kitayama T., Komatsu K., Hattori M., Matsuo H., Oshima T., Suto Y. & Yoshikawa K. 2008, arXiv:0805.0500
Read A. M. & Ponman T. J. 2003, A&A, 409, 395
Roettiger K., Burns J. O., Stone J. M., 1999, ApJ, 518, 603
Rossetti, M. & Molendi, S. 2004, A&A, 414, L41
Rottgering H. J. A., Wieringa M. H., Hunstead R.W., & Ekers R. D., 1997, MNRAS, 290, 577
Sarazin C. L. 1988, X-ray emission from clusters of galaxies, (Cambridge University Press)
Sarazin C. L. 1999, ApJ, 520, 529
Serlemitsos P.J., et al. 2007, PASJ, 59, 9
Shafer, R. A. 1983, PhD. Thesis, University of Maryland
Snowden, S. L., McCammon, D., Burrows, D. N., & Mendenhall, J. A. 1994, ApJ, 424, 714
Sodre L. Jr., Capelato H. V., Steiner J. E., Proust D., & Mazure A. 1992, MNRAS, 259, 233
Struble M. F. & Rood H. J. 1999, ApJ, 125, 35
Takahashi T., et al. 2007, PASJ, 59, 35
Takahashi T., Mitsuda K. & Kunieda H. 2006, SPIE proc., 6266
Takizawa M. 2000, ApJ, 532, 183
Tawa N. et al. 2008, PASJ, 60, 11
Vikhlinin A., Markevitch M., & Murray S. S. 2001, ApJ, 551, 160
Vikhlinin A., Markevitch M., & Murray S. S. 2001, ApJ, 549, L47
Watanabe M., Yamashita K., Furuzawa A., Kunieda H., Tawara Y. & Honda H. 1999, ApJ, 527, 80
Wik D. R., Sarazin C. L., Finoguenov A., Matsushita K., Nakazawa K. & Clarke T. E. submitted to ApJ